

Understanding the PSCz Galaxy Power Spectrum with N-body Simulations

Mark C. Neyrinck^{1,3}, Andrew J.S. Hamilton^{1,3}, and Nickolay Y. Gnedin^{2,3}

¹*JILA, University of Colorado, Boulder, CO 80309*

²*Center for Astrophysics and Space Astronomy, University of Colorado, Boulder, CO 80309*

³*Department of Astrophysical and Planetary Sciences, University of Colorado, Boulder, CO 80309*

email: Mark.Neyrinck@colorado.edu

2003 August 28

ABSTRACT

By comparing the PSCz galaxy power spectrum with the results of nested pure dark-matter N-body simulations, we try to understand how infrared-selected galaxies populate dark-matter haloes, paying special attention to the method of halo identification in the simulations. We thus test the hypothesis that baryonic physics negligibly affects the distribution of galaxies down to the smallest scales yet observed. We are successful in reproducing the PSCz power spectrum on scales $\lesssim 40 h \text{ Mpc}^{-1}$, near our resolution limit, by imposing a central density cutoff on simulated haloes, which gives a rough minimum mass and circular velocity of haloes in which PSCz galaxies formed.

Key words: large-scale structure of the universe – galaxies: haloes – cosmology: theory – galaxies: infrared – galaxies: formation – methods: N -body simulations.

1 INTRODUCTION

The distribution of ice in the ocean can be difficult to study when only the tips of icebergs can be observed. We can catalogue the positions and redshifts of galaxies, and can obtain glimpses of the intergalactic environment by observing the Lyman-alpha forest, but the dark matter, the component which plays the largest role in our current paradigm of structure formation, remains obscure. In this paper, we try to connect underlying dark-matter ice to the iceberg tips (galaxies) we can see.

Only in the last few years have we claimed to have a successful cosmological model, the ‘concordance’ Λ CDM model. Its loose ends do seem tieable, but some areas remain largely mysterious: for example, the formation of galaxies within dark-matter haloes, and the resulting relationship between them at the present epoch. Here, we investigate this relationship through their distributions, most succinctly quantified by the power spectrum, or its Fourier dual, the correlation function. Currently, the most extensive measurement of a power spectrum of observed galaxies, ranging over 4.5 decades of wavenumber, is by Hamilton & Tegmark (2002, hereafter HT). It was made from the PSCz (Point Source Catalogue Redshift) catalogue (Saunders et al. 2000) of galaxies observed with the *IRAS* infrared satellite. There will soon be a flood of galaxy clustering data, for example from the Sloan Digital Sky Survey (SDSS, York et al. 2000) and the Two-Degree Field (Lewis et al. 2002) survey. Early data (e.g. Zehavi et al. 2002, Percival et al. 2001) suggest that clustering properties vary with galaxy morphology, lu-

minosity, and colour. Here we restrict ourselves to PSCz infrared galaxies, but with excellent optical data differentiated by colour, an approach such as ours will soon be able to say more about the types of galaxies which inhabit different sorts of dark-matter haloes.

As with other measurements of galaxy power spectra, for example from the APM galaxy survey (Baugh 1996), HT found a roughly power law form. This is strikingly different from the dark matter power spectrum in the current concordance Λ CDM cosmological model. Figure 1 shows the PSCz power spectrum along with linear and non-linear power spectra for the concordance Λ CDM model, and also dark matter power spectra from our simulations. The non-linear dark matter spectrum traces the linear spectrum at large scales, but at smaller, non-linear scales, it rises above it because waves on the scale of collapsing structures grow faster than waves in the linear regime. At even smaller scales, virialization slows growth, producing a downward inflection.

The galaxy and dark-matter power spectra thus appear to be biased with respect to each other (i.e. they are different); their different shapes indicate that bias is scale-dependent. Numerous attempts have been made to understand this. The halo model of large-scale structure (reviewed by Cooray & Sheth, 2002) assumes the existence of small, bound objects (haloes) which are clustered according to the linear power spectrum. Galaxy clustering statistics such as the correlation function can then be calculated as the sum of two terms describing pairs of galaxies from the same and from different haloes. This can make use of a Halo Occu-

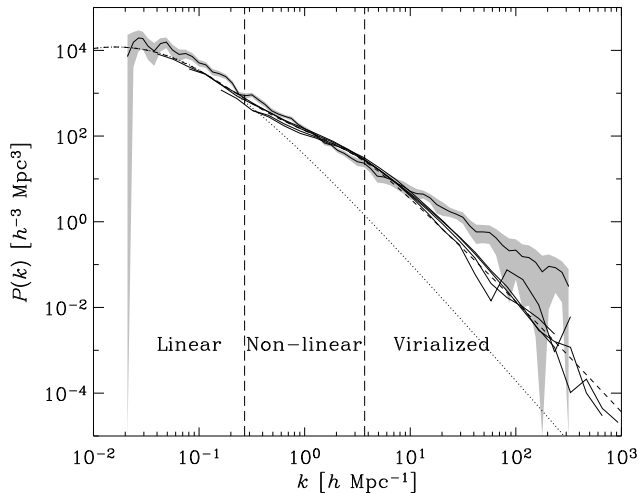


Figure 1. Comparison of the dark matter power spectra from the simulations (thin solid curves) to the linear power spectrum (dotted curve) and, for the sake of illustration, an estimate of the non-linear power spectrum (dashed curve) evolved from the linear power spectrum using the method of Peacock & Dodds (1996). The PSCz power spectrum also appears, surrounded by a grey band. The boundaries of the ‘non-linear’ range of wavenumber were placed by hand, approximately at the two inflections in the dark-matter power spectrum.

pation Distribution, HOD (Benson 2001; White, Hernquist & Springel 2001; Berlind & Weinberg 2002; Berlind et al. 2002), which describes the number of galaxies which inhabit a halo of a given mass. In this context, a halo is defined as a region at least 200 (typical of virialization) times more dense than the background. The approximations of the halo model permit analytic models for the bias between galaxies and dark matter (e.g. Seljak 2000; Sheth & Jain 2002). Recently, a slight but statistically significant deviation from a power law in the projected correlation function of a preliminary SDSS sample was successfully modelled using a HOD in the halo model (Zehavi et al. 2003).

Semi-analytic galaxy formation models (e.g. White & Frenk 1991; Kauffmann et al. 1999; Benson et al. 2000; Somerville et al. 2001, Mathis et al. 2002) and hydrodynamic simulations (e.g. Katz, Hernquist & Weinberg 1992; Cen & Ostriker 2000; Davé et al. 2000; Pearce et al. 2001; White, Hernquist, & Springel 2001; Yoshikawa et al. 2001) have also been successfully applied to the problem of bias. While these approaches attempt to give the relationship between galaxies and dark matter directly, some of the galaxy formation prescriptions in semi-analytic models can be rather ad hoc, and it is not clear that hydrodynamic simulations correctly treat every piece of relevant baryonic physics.

In this paper, we take a different tack: we directly fit the PSCz power spectrum to dark-matter-only N-body simulations. We are thus seeing how far we can take the assumption that on intergalactic scales, baryonic physics negligibly affects the clustering of haloes which contain observed galaxies. Similar studies, without fitting to specific observations, and using different halo-finding algorithms, have been undertaken by Kravtsov & Klypin (1999) and Colín et al. (1999).

We also do not employ a HOD framework. Such a statistical placement of galaxies in haloes is useful in constructing an analytic model or when faced with poor resolution, and can aid intuition. Our approach is more direct: if a halo is defined not as a region above a certain overdensity, but as a region gravitationally bound to a significant maximum in the density field, a definition which would admit subhaloes without their parent haloes, then the number of galaxies detected by a redshift survey inside a halo is either zero or one.

We pay particular attention to the halo-finding algorithm we use to go from a dark matter distribution to a distribution of haloes, and to the effects of resolution on the algorithm. This is the most nontrivial step in comparing the results of simulations to the observed galaxy power spectrum, so it is important to be careful.

2 METHOD

2.1 The Simulations

The PSCz power spectrum spans 4.5 decades of wavenumber; to replicate this dynamic range in an N-body simulation with sufficient mass resolution would be unfeasible. For this reason, and also to test for resolution effects, we ran four manageably sized 256^3 -particle simulations, of comoving box size 32, 64, 128, and $256 h^{-1}$ Mpc, with an adaptive P³M code (Bertschinger 1991). A simulation of box size less than about $32 h^{-1}$ Mpc would miss significant tidal forces from large-scale fluctuations, and also could not form large clusters that appear with low number densities in nature. The values of cosmological parameters we used in the simulation were from the concordance model of Wang, Tegmark & Zaldarriaga (2002): $\Omega_m = 0.34$, $\Omega_\Lambda = 0.66$, $h = 0.64$, and $n = 0.93$. We calculated the transfer function of the initial conditions with the code of Eisenstein & Hu (1999), which returned a value of $\sigma_8 = 0.63$, the rms fluctuation of mass in spheres of radius $8 h^{-1}$ Mpc.

There were two resolution issues to consider: mass resolution and spatial resolution. The mass resolution, i.e. the mass of a particle in the simulation, depends on the number of particles per unit volume. (See Table 2 for particle masses for each simulation.) So, the mass resolution in the four simulations necessarily changes with box size. However, we decided to use the same spatial resolution (softening length) for all simulations: $10 h^{-1}$ kpc, roughly the lowest scale probed in the PSCz power spectrum.

Unlike many cosmological simulations, our softening length was fixed in physical, not comoving (Eulerian, not Lagrangian), coordinates. This means that at early epochs, the comoving softening length was larger, at maximum about $1/6$ the mean interparticle separation in the $32 h^{-1}$ Mpc simulation, and less by factors of two in the others. The first haloes to collapse at $z \approx 10$ turn out to be quite important in determining the fine structure of haloes at $z = 0$. The first haloes contain only a few particles at $z \approx 10$, and a small comoving smoothing length can make their relaxation times tiny, resulting in an overproduction of small, relaxed structures (Moore 2001; Binney & Knebe 2002). By having a fairly large comoving softening length at early times, we hope to have mitigated this problem.

Table 1. Choice of initial conditions. Both the PSCz galaxy density and the ‘Simulation’ dark matter density are normalized to one.

	PSCz	Simulation	PSCz	Simulation
Corner boxes	1.49255	1.11328	0.83325	0.50146
	0.49410	0.76367	0.31982	0.47900
	1.45612	1.20386	2.35201	1.99805
	1.60033	1.63550	0.39196	0.83447
Central box	1.36050	1.10596		

We wanted the four simulated regions to be as similar as possible under the constraints of periodic boundary conditions, enabling us to compare structures in the four simulations to each other. Bertschinger (2001), building on the work of Pen (1997), developed a simple formalism to generate Gaussian random fields with multiple levels of resolution, which we used to nest the initial conditions. Effectively, this means that the phases of fluctuations matched in the centres of each set of initial conditions. An animation depicting the nesting of the boxes can be found at <http://casa.colorado.edu/~neyrinck/nesthalf.mpg>. The zone of agreement between two simulations of box size b and $b/2$ is a central cube of side length roughly $b/4$; a greater zone of agreement is not possible since the smaller box has to obey periodic boundary conditions.

We also selected our initial conditions so that the central region common to the four simulations would have a structure similar to the Local Group and its environs. In this way, we hoped to replicate some features of the way the PSCz observations were made, looking out from the Milky Way, in a slightly overdense region on the outskirts of a modest-sized supercluster. The highest-resolution information in the simulations is from the smallest box, just as the galaxies closest to each other in the PSCz catalogue came from regions close to the Milky Way.

To obtain these special initial conditions, we generated ten sets of initial conditions for a $256 h^{-1}$ Mpc simulation on a 256^3 mesh, and ran them to the present epoch using a (fast but low-resolution) PM code. We counted particles in each cell of side length $8 h^{-1}$ Mpc, the traditional scale of non-linearity, over which we can trust the results of the quick PM code. This gave a 32^3 grid of dark matter density estimates ρ at the present epoch from each set of initial conditions. The same was done for the PSCz catalogue, binning galaxies on a 4^3 grid of $8 h^{-1}$ Mpc cells with the Milky Way at the centre. This resulted in a galaxy number density (n_{PSCz}) grid of total side length $32 h^{-1}$ Mpc, far enough to enclose the local supercluster. We then compared all cubes 4 cells on a side from the simulations to the galaxy density grid. The comparison was made by minimizing the sum of $(\rho - n_{\text{PSCz}})^2$ over nine $16 h^{-1}$ Mpc cubes: eight from dividing the $32 h^{-1}$ Mpc cube into octants, and one more in the centre. We then shifted the best-fitting region to the centre of the $256 h^{-1}$ Mpc set of initial conditions before calculating the lower-box size initial conditions. Table 1 shows these densities for the best fit. Unfortunately, this procedure did not result in structures with obvious visible similarity to the Local Group, but the statistical similarity is reassuring.

Although similar, the inner regions of the four simulations were not identical after evolving them to the present epoch. Large-scale power caused bulk motion in the central region, moving it away and distorting it slightly from its original position. To assess this effect, we approximated

it to first order with the sum of a translation and a linear transformation, an asymmetric tensor which in general could include shear and rotation. We did not use this transformation in any analysis except in evaluating the similarity of the four simulations. The transformation can be written as

$$r_i^{(2)} = C_{ij} r_j^{(1)} + s_i, \quad (1)$$

where $r_i^{(m)}$ is the i th coordinate in the central region of simulation m , C_{ij} is a deformation tensor, and s_i is a translation vector.

Figure 2 shows particles initially in the central $16 h^{-1}$ Mpc box from all simulations in the present epoch. The region from the $32 h^{-1}$ Mpc simulation is untransformed, with the other three regions translated and deformed to fit best on to it. To calculate the shift and deformation, we compared the present-epoch positions of particles which had occupied the same place in the initial conditions; i.e., with the same Lagrangian positions. Since mass resolution changes across simulations, it was necessary to average together positions of particles (in sets of 2^3 , 4^3 , or 8^3) to compare positions in a smaller box size simulation to those in a larger one.

We calculated the translation vector s_i with $\langle r_i^{(2)} - r_i^{(1)} \rangle$, where the angular brackets denote an average over particles. As for the deformation tensor C_{ij} , consider the quantity $\langle (r_i^{(2)} - s_i) r_k^{(1)} \rangle$. Assuming that Eqn. (1) holds, this equals $C_{ij} \langle r_j^{(1)} r_k^{(1)} \rangle$. Thus, where $B_{ik} = \langle (r_i^{(2)} - s_i) r_k^{(1)} \rangle$ and $A_{jk} = \langle r_j^{(1)} r_k^{(1)} \rangle$,

$$C_{ij} = B_{ik} (A^{-1})_{kj}. \quad (2)$$

The translation vectors s_i from the 64, 128, and 256 h^{-1} Mpc simulations to the 32 had magnitudes 2.78, 4.43, and 5.92 h^{-1} Mpc, respectively. The deformation tensors C_{ij} were close to identity matrices, as one would hope; the diagonal elements were all between 0.89 and 1.06 except for one outlier at 0.81, and the off-diagonal elements had magnitudes below (mostly well below) 0.06. With the first-order adjustment, the agreement is still not perfect, but we expect the shear from large-scale waves outside the inner box to change slightly over its length; moreover, slight differences are likely to amplify when non-linearly evolved.

2.2 Halo finding

To compare to the observed galaxy power spectrum, it is necessary first to find haloes in the set of dark-matter particles returned by the simulations. Although they do reasonable jobs, no halo-finding algorithm (HFA) is perfect. In some analyses of N -body simulations, surprisingly little discussion is given of the choice of HFA.

The first step of most HFAs is to estimate the density, a quantity which is not obviously defined given only

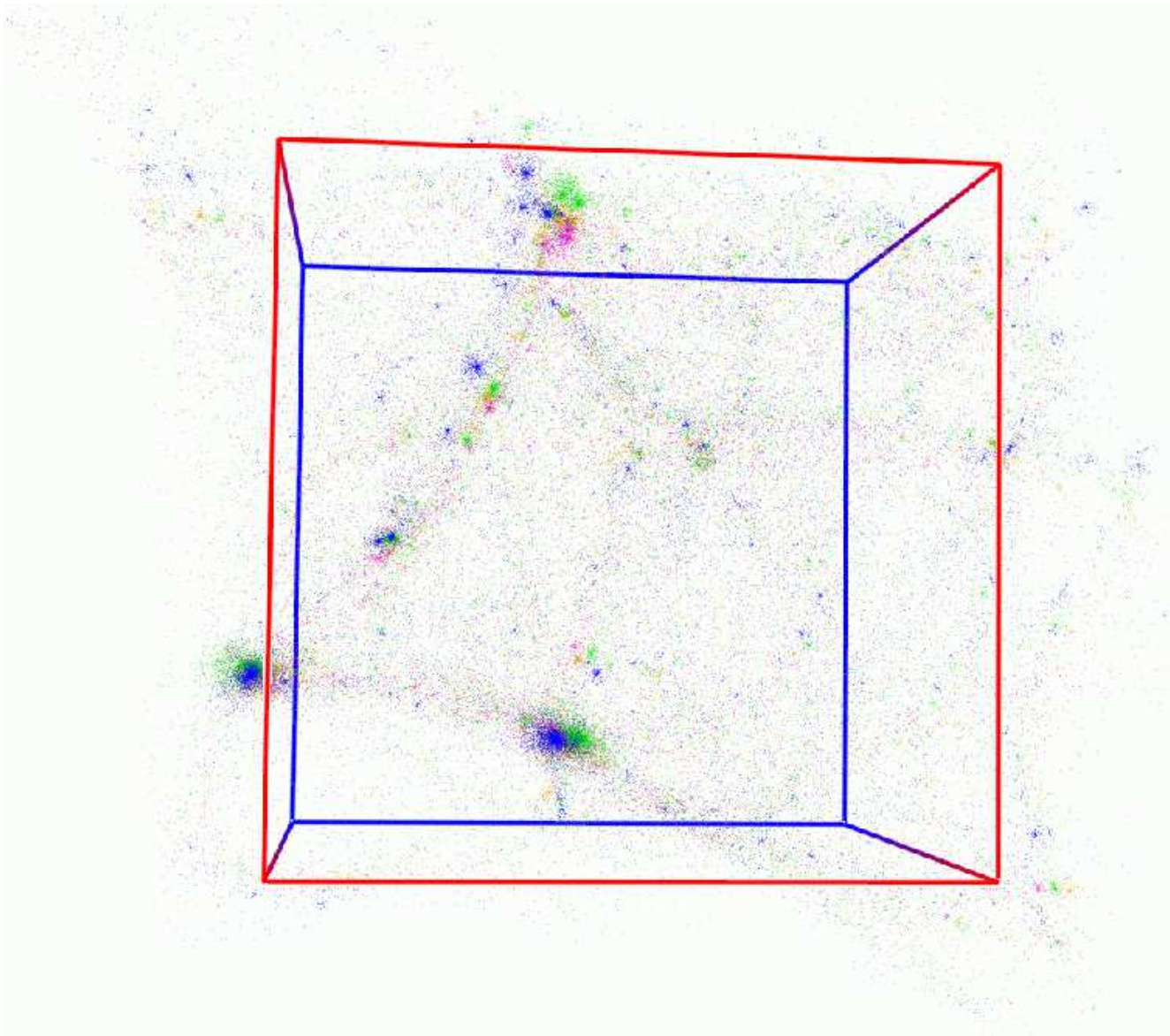


Figure 2. The region originally in the central $16 h^{-1}$ Mpc region of each simulation. Particles from the 32 , 64 , 128 , and $256 h^{-1}$ Mpc simulations appear in magenta, orange, green, and blue, respectively. The sets of particles from simulations of box size greater than $32 h^{-1}$ Mpc have undergone a translation and linear transformation to lie on the set from the (untransformed) $32 h^{-1}$ Mpc simulation. All particles from the central region are shown for the $128 h^{-1}$ Mpc simulation, and the number densities of particles from other simulations are adjusted by factors of eight to match. Thus, $1/8$ and $1/64$ of the particles from the 64 and $32 h^{-1}$ Mpc simulations appear. In the $256 h^{-1}$ Mpc case, the number density was octupled by adding new particles which bisect lines joining particles adjacent on the initial mesh. The predominantly blue character of the large haloes at the bottom arises because the halo in the $256 h^{-1}$ Mpc simulation is simply in front of the others. The figure was produced using Nick Gnedin’s IFRIT visualization tool, at <http://casa.colorado.edu/~gnedin/IFRIT/>.

a set of particles. DENMAX (Bertschinger & Gelb 1991) uses an Eulerian approach, calculating the density on a fine mesh by smoothing each particle with a Gaussian of a fixed size, called the smoothing length, r_{smoo} , on an effectively infinitely fine mesh. A Lagrangian approach (HOP, Eisenstein & Hut 1998) uses a fixed number N_{dens} of nearest-neighbor particles to estimate the density at the position of each particle, and also uses a few other parameters. DENMAX has a fixed spatial resolution, while HOP effectively has a fixed mass resolution. The results of both methods are strongly dependent on their free parameters, r_{smoo} or N_{dens} .

Although DENMAX takes much more time to run than HOP, we ended up using a variant of DENMAX. We found that DENMAX is capable of finding smaller haloes than HOP, down to about ten particles. DENMAX works by moving particles along density gradients until they are at a maximum. It then uses a ‘Friends-of-Friends’ algorithm, finding clusters of moved particles closer than a small linking length ($1/1024$ times the box size) to each other. The last step is to ‘unbind’ iteratively any particles whose energies exceed the escape energy from their haloes. The output of DEN-

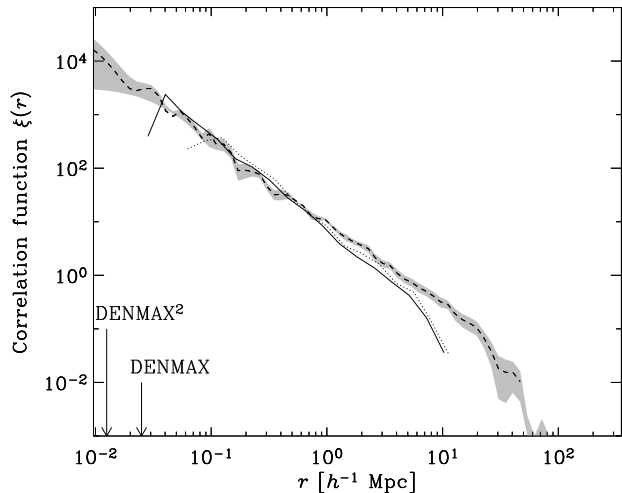


Figure 3. The effect of added DENMAX² haloes on the correlation function in the 32 h^{-1} Mpc simulation. The dashed curve is the PSCz correlation function, and the grey band shows its errors. The dotted curve is the best fit using just DENMAX haloes, and the solid curve is the best fit including DENMAX² haloes. The best-fitting central density cutoff was different in each case: for DENMAX, $\rho_{c,min}$ was 225 particles; for DENMAX², it was 122 particles. The arrows show the DENMAX and DENMAX² smoothing lengths: 0.025 and 0.0125 h^{-1} Mpc, respectively.

MAX is a list of haloes with their masses (number of bound particles), and their position and velocity centroids.

In DENMAX, a large smoothing length smears out close pairs of haloes, while a small smoothing length, with its higher density threshold, fails to include the outskirts of haloes in their mass, and also misses isolated, less-dense haloes. Gelb & Bertschinger (1994) discuss some effects of DENMAX resolution. Empirical tests have indicated that setting $r_{smoo} = 1/5$, in units of the mean interparticle separation, yields a halo mass spectrum similar to that given by the Press–Schechter (1974) formalism, a useful, though not omniscient, guide. This choice of r_{smoo} makes some sense theoretically, too, since the spherical collapse model (Gunn & Gott 1972) predicts that a virialized object is $\delta \approx 180$ times denser than the background in a standard flat ($\Omega_m = 1$) cosmology, and somewhat higher than that in a Λ CDM cosmology. Fiducially, regions of overdensity 200 and above are virialized, corresponding to a smoothing length of $1/200^{1/3}$, about $1/5$.

We applied DENMAX with the canonical smoothing length to the results of each simulation, and calculated halo power spectra. The halo-finding resolution we obtained was rather poor; there was a small-scale downturn in each power spectrum starting at significantly larger scales than the simulation’s softening length. We therefore tried halving the DENMAX smoothing length to $r_{smoo} = 1/10$, which succeeded in extending the power law in the correlation function to smaller scales by about a factor of two. The smaller smoothing length evidently picked out subhaloes which the canonical smoothing length had merged together. A small smoothing length is desirable in detecting subhaloes within a halo, since in a halo, the spatial scales involved are smaller, and the background density is higher.

We wanted to use higher resolution in higher-density regions without forsaking the advantages of the canonical r_{smoo} in lower-density regions. We therefore used an algorithm which we call DENMAX², in which DENMAX is run as normal with the canonical $r_{smoo} = 1/5$, but then is applied to each returned halo separately with $r_{smoo} = 1/10$. Although this factor of two is rather arbitrary, it put the DENMAX² r_{smoo} close to, but still above, the softening length in the 32 h^{-1} Mpc simulation, and it was a convenient choice with so many other factors of two being used, e.g. between the box sizes. We could have kept the DENMAX² r_{smoo} the same in physical units between the boxsizes, but instead fixed it in interparticle units. This was for a couple of reasons: we wanted to hold constant the ratio of the highest and lowest reliably measured wavenumber; also, in the larger-boxsize simulations, a fixed smoothing length in physical units would be tiny in interparticle units, and would thus encounter undesirably high Poisson noise.

Figure 3 shows the effect of extra DENMAX² substructure on the best-fitting (defined below) halo correlation functions in the 32 h^{-1} Mpc simulation; it extends the power law to scales about half as large, as one would expect from the halving of r_{smoo} . The results are promising, but the choices of r_{smoo} for DENMAX and DENMAX² are still arbitrary, indicating the desirability of a HFA without such free parameters.

From the list of DENMAX and DENMAX² haloes, we had to pick a subset which we thought could represent PSCz galaxies. Since DENMAX returns the mass of each halo, this was an obvious property to use to characterize haloes. However, the mass of the largest DENMAX² subhalo is necessarily less than that of its parent DENMAX halo, both because it contains a subset of the parent halo’s particles, and because DENMAX²’s smaller r_{smoo} detects smaller structures. We thus could not compare DENMAX mass and DENMAX² mass directly. We could have tried to ‘correct’ DENMAX² masses to DENMAX levels, which are probably more physically meaningful, since they approximate the virial mass. For example, we could have compared the DENMAX masses of each halo split by DENMAX² to the DENMAX² mass of its largest subhalo. However, it was occasionally unclear which subhalo represented the original halo. Also, it is not obvious that the relationship between DENMAX and DENMAX² masses would be the same for satellite subhaloes and main subhaloes.

We felt it was both simpler and more consistent to fit using another quantifier. Figure 4 shows that the central density of a halo, estimated by counting the number of particles within a fixed radius r_ρ of the halo’s centre of mass as returned by DENMAX, is well-correlated to its DENMAX mass. Also, central density does not unfairly handicap dense but (as detected by DENMAX) unmassive haloes in their quest for inclusion in the halo list. For the 32 h^{-1} Mpc simulation, we used $r_\rho = 20 h^{-1}$ kpc. At twice the softening length, this was about the smallest scale at which we could expect to obtain a meaningful density estimate. Unfortunately, we could not use the same r_ρ for the larger simulations, because the mass resolution became too poor, causing the density estimate within a small region to be dominated by Poisson noise. So, we simply increased r_ρ in proportion to the box size of the simulation.

Another quantity we could have used to characterize

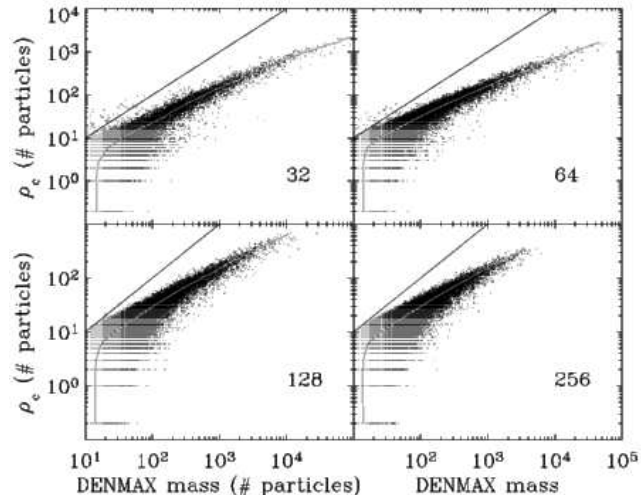


Figure 4. Scatter plots of DENMAX mass (number of particles in the halo) versus central density ρ_c (the number of particles within radius r_ρ) for all simulations. Haloes with $\rho_c = 0$ are shown with $\rho_c = 0.2$. No haloes had a DENMAX mass under 10 because DENMAX discards haloes with less than 10 particles. The solid grey line passing through the distribution shows the average mass at each ρ_c . To obtain the mass at a particular $\rho_{c,0}$, we averaged together the masses of haloes with ρ_c within $1/10$ of a dex of $\rho_{c,0}$. The thin black line shows the identity function, $y = x$, which would result if all, and only, particles counted in the DENMAX mass were within r_ρ of the halo centre.

haloes is maximum circular velocity v_c . Figure 5 shows a comparison of central density to v_c for DENMAX haloes; the relationship is rather tight. To calculate v_c , we used the procedure employed by the Bound Density Maxima HFA (Klypin et al. 1997). This procedure, described at <http://astro.nmsu.edu/~aklypin/PM/pmcode/node6.html>, yields $v_c = \sqrt{GM(r)/r}$, evaluated at the radius of the first concentric shell about the halo where the overdensity inside dips below 200, and also checks its spherically averaged density profile to thwart structures hoping to inflate v_c for nearby haloes. The maximum circular velocity is a useful quantity because it can seemingly be related to observed galactic circular velocities. However, it is fallible, relying as it does on spher averaged density profiles. In any case, the relationship between the two quantities is quite tight, so they are roughly interchangeable.

We thus picked subsets of the halo list according to a lower density cutoff $\rho_{c,min}$; it is physically reasonable that the central density in a halo must exceed some threshold to house an observed galaxy. We first imposed the density cutoff on the list of DENMAX haloes. If application of DENMAX² split a halo in the resulting subset into subhaloes, we imposed the density cutoff on each of the subhaloes. If none of these subhaloes exceeded the density cutoff, the original halo stayed in the list; otherwise, any dense-enough subhaloes (which almost always include the original) replaced the original halo in the list.

We then calculated the haloes’ power spectrum by binning halo pairs by their separation, and then submitting the resulting correlation function to an FFT (actually FFTLog, Hamilton 2000). We also tried two other methods. In the

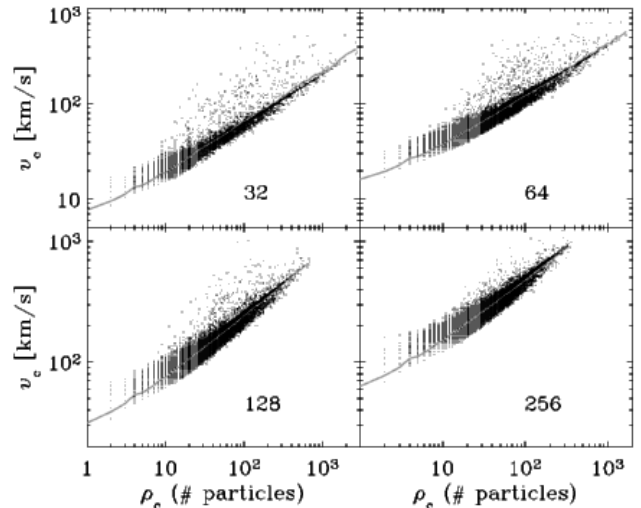


Figure 5. Scatter plots of central density ρ_c versus maximum circular velocity v_c for all DENMAX haloes. The solid grey line passing through the distribution shows the average v_c at each ρ_c . To obtain v_c at a particular $\rho_{c,0}$, we averaged together v_c ’s of haloes with ρ_c within $1/10$ of a dex of $\rho_{c,0}$.

first, we calculated the density on a mesh, using the Nearest Grid Point interpolation scheme, and found the power spectrum using a 3D FFT. To get to the smallest scales, Klypin (private communication, 2001) pointed out that if one divides a box of particles into octants (or some other number of equal parts), and overlays all of the octants on each other, periodic boundary conditions will still be satisfied, and the power spectrum of the condensed box should be the same as that of the larger box. This approach did work rather well, but there were small discrepancies between power spectra from different octant overlayings, and it was not obvious how to combine them. Another method we tried used an unequally spaced FFT (Beylkin 1995), which uses multiresolution analysis (wavelets) to calculate the exact FFT of a set of delta functions in mass (i.e. particles), but a sufficiently large unequally spaced FFT required more memory than was convenient. These other methods agreed well with the correlation function technique, but we ended up using the correlation function technique because it is possible to calculate the exact correlation function of a relatively small number of haloes quickly with no resolution limit. Also, this technique is not subject to the vagaries of window functions which exist for standard FFTs.

While it is more direct to calculate a correlation function than a power spectrum from a simulation, the opposite is true for a redshift survey such as PSCz. This is because the power spectrum in directions transverse to the line of sight in a redshift survey is unaffected by redshift distortions, which is not true for the correlation function. So, in comparing simulations to observations, it was always necessary to translate one set of data into the same space (either real or Fourier) as the other. Empirically, the correlation function varied more dramatically on the small-scale end with the density cutoff $\rho_{c,min}$, and also it is easier to interpret directly in terms of physical pairs of haloes, so we used the correlation function for fitting. It would have been better in principle to

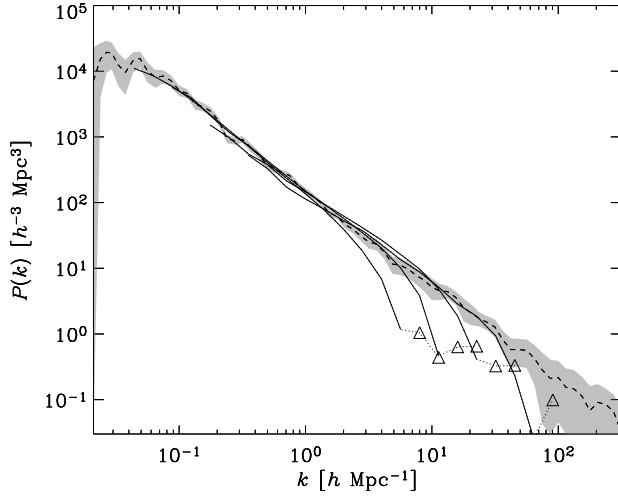


Figure 6. The best-fitting power spectra (see Fig. 13 for error bars) for all simulations. The PSCz power spectrum is the dashed curve with a grey error band; the best fits from the (from left to right) 256, 128, 64, and 32 h^{-1} Mpc simulations appear as solid curves. Triangles connected with dotted lines denote negative values.

use the errors in the power spectrum, since they are more directly measured from PSCz. However, HT have not at present found a positive-definite covariance matrix for the PSCz power spectrum. Thus any comparison we make to simulations would not be completely rigorous anyway. We were still able to estimate the goodness of fit by ignoring cross-correlations among data points (just using HT’s error bars), making a ‘pseudo- χ^2 ’ ($\tilde{\chi}^2$) statistic. Where ξ denotes the correlation function, and b is the box size of a simulation, we included $\xi(r)$ ’s with r between $b/256$ and $b/2$; with our bins r_i varying as they did by a factor of $\sqrt{2}$, this included 14 points in the fit. We calculated $\tilde{\chi}^2 = \sum_i \left(\frac{\xi(r_i) - \xi_{\text{PSCz}}(r_i)}{\sigma_{\text{PSCz}}(r_i)} \right)^2$, where $\xi_{\text{PSCz}}(r)$ is the PSCz correlation function at r , and $\sigma_{\text{PSCz}}(r)$ is the error in $\xi_{\text{PSCz}}(r) = \left| \frac{\xi_+ - \xi_-}{2} \right|$, the average of the upper and lower error bars as reported by HT. ξ_{PSCz} , ξ_- , and ξ_+ were logarithmically (or linearly, if adjacent data points straddled zero) interpolated if necessary.

3 RESULTS

Figure 6 shows the best individually-fit power spectra from each simulation. The resulting bias factors (see next paragraph) appear in Fig. 8, and the $\tilde{\chi}^2$ curves for the fits appear in Fig. 9. Figure 10 shows the $\tilde{\chi}^2$ curves as a function of halo number density. Figures 7 and 11 show an alternative collective fit, still varying a central density cutoff, but constraining the halo number density to be the same in the smallest three simulations; see §3.1.1 for further discussion. With the first of these fits, we have reproduced the form of the PSCz power spectrum on scales $k \lesssim 40 h \text{ Mpc}^{-1}$, or $r \gtrsim 0.05 h^{-1}$ Mpc. The softening length was $0.01 h^{-1}$ Mpc, so this is not much worse than one would hope for given that haloes are many-particle, extended objects which necessarily exclude each other on scales comparable to their radius. Correlation

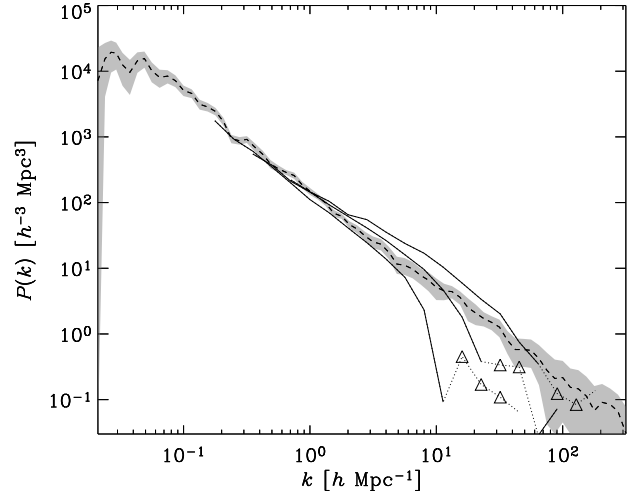


Figure 7. The best-fitting power spectra (error bars are similar to those in Fig. 12) for the 128, 64, and 32 h^{-1} Mpc simulations, constrained so that the halo number density matches. The PSCz power spectrum is the dashed curve with a grey error band. Triangles connected with dotted lines denote negative values.

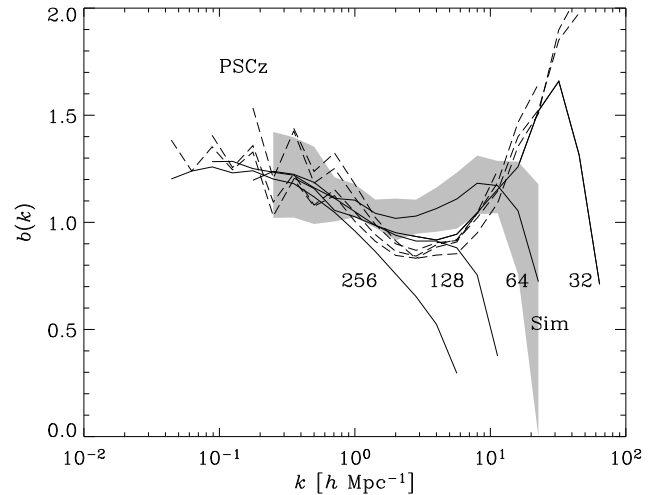


Figure 8. The dashed curves show the bias factors between both the PSCz power spectrum and the dark matter power spectra in each simulation; the solid curves show the bias factors between the haloes and the dark matter in each simulation. The PSCz bias curves are $b_{\text{PSCz}}(k) = \sqrt{P_{\text{PSCz}}(k)/P_{\text{dm}}(k)}$, with a different P_{dm} for each simulation. The simulation bias curves are $b_{\text{sim}}(k) = \sqrt{P_{\text{haloes}}(k)/P_{\text{dm}}(k)}$, again running through the simulations. An error band arising from the errors in the power spectrum in Figure 13 as been put around the 64 h^{-1} Mpc bias curve, representative of the others.

functions and power spectra appear with their theoretical error bars in Figs. 12 and 13. The correlation functions turn down at large scales because waves start to damp out as one approaches half the box size. These figures also show the dark matter correlation functions from each simulation; see Fig. 8 for a clearer view of their relationships. The error bars in the correlation function were calculated by splitting the

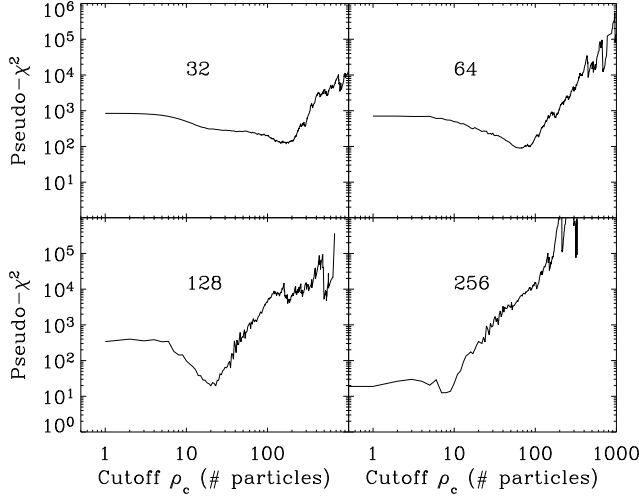


Figure 9. $\bar{\chi}^2$ values for the four simulations as functions of central density cutoff $\rho_{c,min}$. In the $256 h^{-1}$ Mpc simulation, the $\bar{\chi}^2$ value at $\rho_{c,min} = 0$ (including all detected haloes) is shifted to $\rho_{c,min} = 0.5$ so that it can appear on a log-log plot.

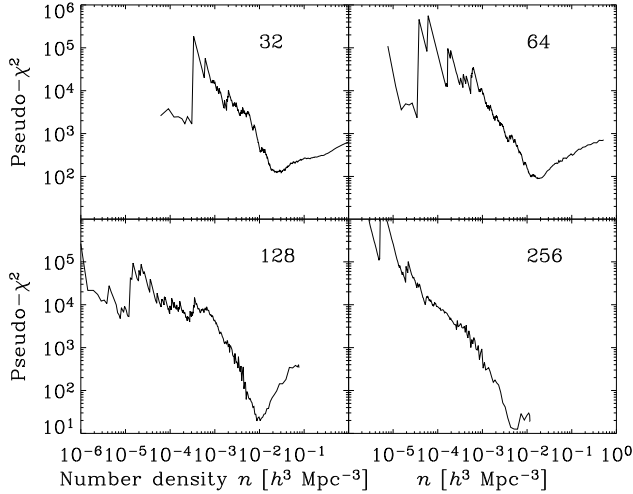


Figure 10. $\bar{\chi}^2$ values for the four simulations as functions of halo number density. The best-fitting number densities are 0.0244, 0.0175, 0.00873, and 0.00611 haloes per h^{-3} Mpc³ for the 32, 64, 128, and $256 h^{-1}$ Mpc simulations, respectively.

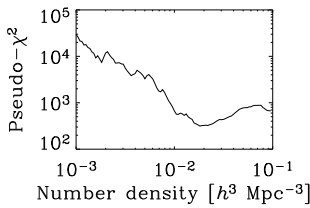


Figure 11. The sum over the smallest three simulations of $\bar{\chi}^2$ as a function of halo number density. The best fit is at 0.0182 haloes per h^{-3} Mpc³, which corresponds to the PSCz galaxy number density at a depth of about $20 h^{-1}$ Mpc.

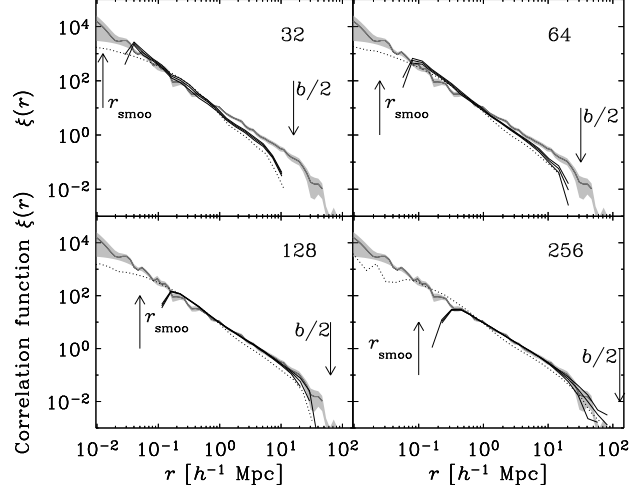


Figure 12. The best-fitting halo correlation functions (thick solid curves) shown individually with error bands (thin solid curves). The PSCz correlation function appears as a light curve with grey error bands, and the simulations' dark matter correlation functions appear as dotted curves. Arrows show the scales of the DENMAX² smoothing length r_{smoo} ($b/2560$), and half the box size ($b/2$), where the correlation function in a box of size b becomes meaningless. All softening lengths were $0.01 h^{-1}$ Mpc.

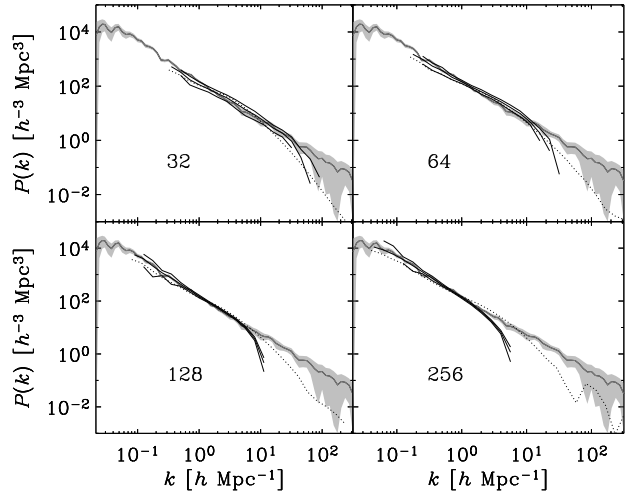


Figure 13. The best-fitting halo power spectra (thick solid curves) shown individually with error bands (thin solid curves). The PSCz power spectrum appears as a light curve with grey error bands, and the simulations' dark matter power spectra appear as dotted curves.

simulation volume into octants and calculating correlation functions in each. The error at $\xi(k)$ is then $\sqrt{[\text{Var}(\xi_i(k))]/8}$, where i runs over all octants. The same technique was used to calculate power spectrum error bars.

Figure 8 shows a plot of the bias factor $b(k) = \sqrt{P_{\text{haloes}}(k)/P_{\text{dm}}(k)}$, a measure of the difference between the galaxy and dark matter power spectra, for the four simulations. The small-scale downturns are caused by the resolution of the halo-finding algorithm in each spectrum. The

Table 2. Fit Information.

Box size b [h^{-1} Mpc]	32	64	128	256
Particle mass [$10^8 h^{-1} M_{\odot}$]	1.8	15	120	940
Halo mass m_b [# particles]	764 ± 322	269 ± 121	71 ± 31	17 ± 8
Halo mass ratio m_b/m_{2b}	2.8 ± 1.8	3.8 ± 2.4	4.2 ± 2.7	
Physical halo mass [$10^{11} h^{-1} M_{\odot}$]	1.4 ± 0.6 ,	4.0 ± 1.8	8.4 ± 3.7	16 ± 8
Circular velocity v_c [km/s]	72 ± 28	98 ± 24	112 ± 14	120 ± 13
Halo number density [$h^3 \text{Mpc}^{-3}$]	0.0244	0.0175	0.00873	0.0061
$\rho_{c,min}$ [# particles]	122	66	22	6

shape of the bias function is similar to what Kravtsov & Klypin (1999) found; the dependence of bias on scale must be similar to this to achieve a power-law form in the galaxy power spectrum, given the inflection in the dark matter power spectrum caused by the onset of non-linearity, and the turnover back at smaller scales due to virialization.

Table 2 shows the central density cutoffs of the best fits, along with the number densities of the best-fitting populations, and effective cutoffs in halo mass (from Fig. 4) and maximum circular velocity (from Fig. 5). The quoted errors are the standard deviations in mass or v_c of haloes with ρ_c within 1/10 of a dex of $\rho_{c,min}$. We ignore errors arising from the goodness-of-fit, which we did not include since our $\tilde{\chi}^2$ estimate is not rigorous. These errors could be sizable, though, particularly in the $256 h^{-1}$ Mpc simulation. The minimum at 6 particles in Fig. 9 for the $256 h^{-1}$ Mpc simulation’s haloes is quite shallow. The $\tilde{\chi}^2$ value including all detected haloes ($\rho_{c,min} = 0$) was only slightly greater than at $\rho_{c,min} = 6$. Using either cutoff, most of the haloes are right at the detection limit (a DENMAX mass of 10 particles), so it is quite possible that the mass resolution in this simulation is insufficient to pick up the truly best-fitting population of haloes.

3.1 Discussion

Figure 6 shows good fits to the PSCz power spectrum for each simulation, but the question remains: could these haloes from four different simulations represent the same set of haloes? Encouragingly, when translated into maximum circular velocity, the cutoff intervals mostly overlap with each other. The only disjoint error intervals are between the 256 and the $32 h^{-1}$ Mpc simulations, and once again, the errors in the $256 h^{-1}$ Mpc case are probably underestimated. However, we do not expect them to be exactly the same populations, since in a smaller box, the higher mass and DENMAX² spatial resolutions produce more haloes with small separations, many of which could join together in a lower-resolution simulation; this fact is evident in the increased small-scale range of the correlation functions in each simulation. Still, there are two apparent discrepancies which should be understood in Table 2: in halo number density and in implied mass cutoff.

One possible explanation for the different-looking halo populations is cosmic variance; i.e. that our chosen set of initial conditions was funny in some way. For example, because of periodic boundary conditions, the $32 h^{-1}$ Mpc simulation is not big enough to contain the local supercluster from the PSCz cube we used to pick the initial conditions. We measured the correlation functions of haloes in the central $16 h^{-1}$ Mpc cube of each simulation, first applying the shifts and deformation tensors necessary to put the larger simula-

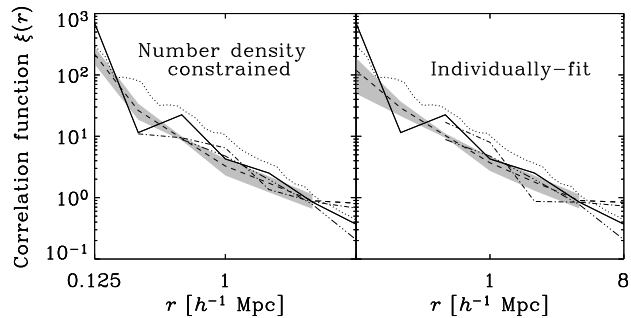


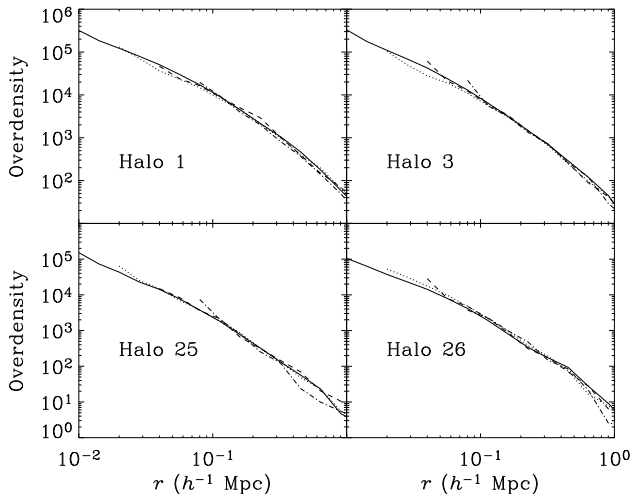
Figure 14. Best-fitting halo correlation functions measured from the central cube of length $16 h^{-1}$ Mpc from each simulation, when constrained to have matching number densities and when individually fit. The larger halo sets have been mapped using the shift and deformation described at the end of §2.1 onto the $32 h^{-1}$ Mpc central region before finding the correlation function. To boost the number of pairs, we actually calculated the cross-correlation of haloes in the central boxes with all haloes in the box in each case. The PSCz correlation function is the dotted curve, and correlation functions from the 32, 64, 128, and $256 h^{-1}$ Mpc simulations appear as solid, dashed, dashdotted, and dashdotdotted curves, respectively. We have put error bands (measured as previously by dividing the region into octants) around the $64 h^{-1}$ Mpc correlation function, which are typical of the others.

tions on top of the $32 h^{-1}$ Mpc simulation. Figure 14 shows the results of this test, for both the individually-fit and number density-constrained central density cutoffs. The central box is evidently undercorrelated relative to the larger boxes, but the correlation functions from different simulations seem consistent with each other, even when the sets of haloes are constrained to have the same number density.

To try to understand the behavior of DENMAX mass and halo number density across the simulations, we identified a few haloes by eye in the central regions of the four simulations. We looked for large haloes near each other across the simulations, and then visualized them with the `points` program written by Michael Blanton, at <http://physics.nyu.edu/~mb144/graphics.html>. Identifying the same halo in each simulation was complicated by the bulk motion and distortion of the central regions, as discussed at the end of §2.1. We found four obvious haloes; the numbers of particles which comprised them in the $256 h^{-1}$ Mpc simulation were 636, 501, 100, and 89. Figure 16 shows one of them (‘Halo 3’ from Table 3), and how it was split by DENMAX². While the results across simulations are similar, some subhaloes appear differently in different simulations, and some of them are questionably existent. If subhaloes have orbited their parent halo a few times, they might not be in the same place across all simulations, since

Table 3. Splitting of the same haloes with decreasing box size (and thus decreasing DENMAX² smoothing length). The halo number is the mass rank in the 32 h^{-1} Mpc simulation DENMAX list, and b denotes the box size, in h^{-1} Mpc.

b	Halo 1	Halo 3	Halo 25	Halo 26
32	55	55	29	25
64	19	20	9	10
128	4	3	6	3
256	2	1	1	1

**Figure 15.** Density profiles, as a function of distance from their DENMAX centres, of the four haloes identified across the simulations. The solid, dotted, dashed, and dashdot curves are from the 32, 64, 128, and 256 h^{-1} Mpc simulations, respectively. The halo appearing in Fig. 16 is in the bottom-right corner.

the simulations do quite well in tracking orbits, but not necessarily phases along them. Figure 15 shows density profiles for the four haloes identified across the simulations, which agree quite well. In the next two sections, we will discuss what we learned from these haloes.

3.1.1 Number Density

From Table 2, the number density of best-fitting haloes changes by a factor approaching two between adjacent simulations. To gauge the severity of this potential problem, we investigated the effect of forcing the number density of haloes in each box to match. Figure 10 shows $\tilde{\chi}^2$ as a function of halo number density. Excluding the 256 h^{-1} Mpc simulation because it was not clear that the desired set of haloes was well-resolved, and adding together $\tilde{\chi}^2$ values from other simulations with equal weight, we obtained a total $\tilde{\chi}^2$ curve, which appears in Fig. 11. The best-fitting number density from Fig. 11 was $0.0182 h^{-3} \text{ Mpc}^3$, which matches the number density of PSCz galaxies that are about 20 h^{-1} Mpc from the Milky Way. Figure 7 shows the resulting power spectra, which are not particularly consistent, either with each other or with PSCz. The number density constraint allows smaller haloes into the 128 h^{-1} Mpc set, which lowers the power spectrum; it has the opposite effect on the 32 h^{-1} Mpc set, removing smaller haloes and lifting the power spectrum.

However, it is not obvious that we should expect the

same number density of haloes when resolution changes. Suppose we have a set of N haloes in a box of volume V . To measure the correlation function, we bin pairs of haloes by distance r_i to obtain $P(r_i)$, the number of pairs in bin i , with volume $V(r_i)$. The value of the correlation function $\xi(r_i)$ in bin i is then given by:

$$1 + \xi(r_i) = \frac{V}{V(r_i)} \frac{P(r_i)}{N^2}. \quad (3)$$

The RHS expresses the number of halo pairs in a bin, normalized by dividing by three quantities: the volume of the bin, the number of haloes, and the mean halo number density. Now suppose that each of these haloes in fact consists of two subhaloes which become resolved when the resolution increases, and that all separations between these subhaloes are much smaller than the r_i 's. Each pair turns into four, and N doubles. The new correlation function ξ' over the previous range of r_i 's is given by

$$1 + \xi'(r_i) = \frac{V}{V(r_i)} \frac{4P(r_i)}{(2N)^2} = 1 + \xi(r_i), \quad (4)$$

and pairs also appear in new, smaller-scale bins, imparting to the correlation function there a value possibly as large as the other $\xi(r_i)$'s, depending on the bin size and distribution of subhalo distances. So in this simple case, when a higher spatial resolution reveals more substructure, the halo number density increases without changing the correlation function except in new, smaller-scale bins.

Might this model resemble our simulations? Table 3 shows how the number of subhaloes uncovered by DENMAX² changes with box size for the four haloes we identified. This table includes all subhaloes, not merely the ones which make the central density cutoff. Also, these are relatively large parent haloes, more likely to have substructure than smaller ones. This seems to be a reasonable explanation for the change in halo number density across the simulations.

3.1.2 Mass cutoff

Where m_b is the DENMAX mass (in number of particles) of a halo in a simulation of box size b , m_b/m_{2b} should ideally be 8, the same factor by which the mass resolution changes. The values of m_b/m_{2b} for the best fits in Table 2 fall well short of this. For our four-halo sample, $m_{32}/m_{64} = 6.3 \pm 0.8$, $m_{64}/m_{128} = 6.1 \pm 0.6$, and $m_{256}/m_{128} = 7.3 \pm 0.5$, somewhere between the ratios in Table 2 and the expected value of 8. The shrinkage of a halo with increased mass resolution is obvious in Fig. 16, and comes primarily from the reduction in r_{smoo} in physical units as particle mass decreases.

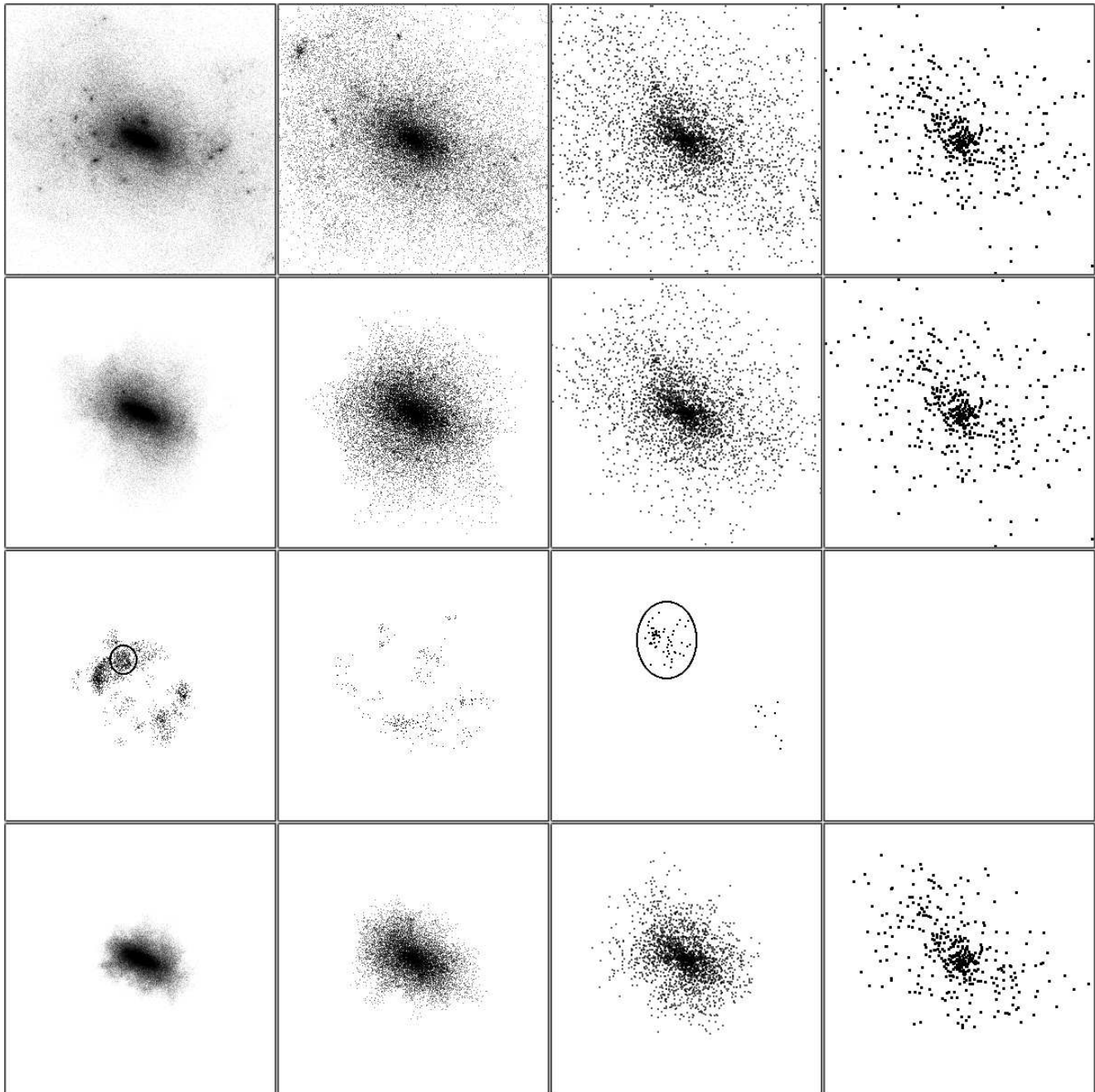


Figure 16. Comparison of a halo (the third-largest in the $32 h^{-1}$ Mpc simulation, with a mass of a few times $10^{13} M_{\odot}$) in different simulations, and the effect of DENMAX² on it. The first row shows all particles, whether they were detected by DENMAX or not, in a box $1.8 h^{-1}$ Mpc on a side around the center of the halo, in, from left to right, the 32, 64, 128, and $256 h^{-1}$ Mpc simulations. The second row shows particles in the halo as detected by DENMAX. Note that there are many evident ‘subhaloes’ which do not appear in the second row; these were already detected as different individual haloes by DENMAX, before application of DENMAX². DENMAX² split the DENMAX halo into 55, 20, 3, and 1 subhalo(es) in the 32, 64, 128, and $256 h^{-1}$ Mpc simulations, respectively. The satellite subhaloes appear in the third row, with circles around the subhaloes (one in each of the 128 and $32 h^{-1}$ Mpc simulations) satisfying the central density cutoff. The final row shows the main subhalo (also satisfying the central density cutoff) as detected by DENMAX². Note the physical enlargement of the halo with boxsize; this is a result of the increase in the smoothing length in physical units. The figure was produced using Nick Gnedin’s IFRIT visualization tool, at <http://casa.colorado.edu/~gnedin/IFRIT/>.

4 CONCLUSIONS

We have shown that we can reproduce the clustering properties of infrared-selected PSCz galaxies fairly well in simulations for scales $k \lesssim 40 h \text{ Mpc}^{-1}$, near our resolution limit,

by imposing a central density cutoff on haloes. This central density cutoff implies a rough dark matter mass cutoff in PSCz galaxies of $10^{11-12} M_{\odot}$, and a cutoff in maximum circular velocity of roughly 100 km/sec. Thus, it appears that dark matter physics alone is sufficient to describe the

distribution of PSCz galaxies on the scales we probed. It is doubtful that there is a strict central density cutoff in haloes which house PSCz galaxies in nature, but it seems that central density is still a decent indicator of the hospitality of haloes toward nascent galaxies. While the fits look good, their full statistical assessment awaits a covariance matrix for the PSCz power spectrum.

We have also found that the best-fitting halo populations from the four simulations are probably consistent with each other. Their circular velocities are roughly consistent. On the other hand, their number densities and mass cutoffs do not increase systematically with spatial resolution, but we do not believe that these discrepancies indicate that the populations are necessarily inconsistent. One might in fact expect the halo number density to increase when higher resolution reveals more substructure, without affecting the correlation function. Also, the varying mass cutoff is at least partially an artifact of our halo-finding algorithm. We are currently considering new methods to identify haloes with fewer (perhaps even zero) free parameters, which we hope will coax the tips more confidently from their simulated dark-matter icebergs.

5 ACKNOWLEDGMENTS

This work was supported by NASA ATP grant NAG5-10763, and a grant on the Origin 2000 system by the National Computational Science Alliance. We thank an anonymous referee for helpful and insightful comments and suggestions. The work also advanced pleasantly at the Aspen Center for Physics.

REFERENCES

- Baugh C., 1996, MNRAS, 280, 267
 Berlind A.A. et al., 2002, submitted to ApJ. (astro-ph/0212357)
 Berlind A.A., Weinberg D.H., 2002, ApJ, 575, 587
 Benson A.J., 2001, MNRAS, 325, 1039
 Benson A.J., Cole S., Frenk C.S., Baugh C.M., Lacey, C.G., 2000, MNRAS, 311, 793
 Bertschinger E., 1991, in Holt S., Trimble V., Benett C., eds, After the First Three Minutes. AIP, New York, p. 297
 Bertschinger E., 2001, ApJS, 137, 1
 Bertschinger E., Gelb J.M., 1991, Computers in Physics, 5, 164
 Beylkin G., 1995, Applied and Computational Harmonic Analysis, 2, 363
 Binney J., Knebe A., 2002, MNRAS, 333, 378
 Cen R., Ostriker J.P., 2000, ApJ, 538, 83
 Colín P., Klypin A., Kravtsov A., Khokhlov A., 1999, ApJ, 523, 32
 Cooray A., Sheth R., 2002, Phys. Rept. 372, 1
 Davé R., Hernquist L., Katz N., Weinberg D., 2000, in Mazure A., Le Fèvre O., Le Brun V., eds, ASP Conference Series, Vol. 200, Clustering at High Redshift, p. 402
 Eisenstein D.J., Hu W., 1999, ApJ, 511, 5
 Eisenstein D.J., Hut P., 1998, ApJ, 498, 137
 Gelb J., Bertschinger E., 1994, ApJ, 436, 467
 Gunn J.E., Gott J.R. III, 1972, ApJ, 539, 39
 Hamilton A.J.S., 2000., MNRAS, 312, 257
 Hamilton A.J.S., Tegmark M., 2002, MNRAS, 330, 506
 Katz N., Hernquist L., Weinberg D.H., 1992, ApJL, 399, 109
 Kauffmann G., Colberg J.M., Diaferio A., White S.D.M., 1999, MNRAS, 303, 188
 Klypin A.A., Gottlöber S., Kravtsov A., Khokhlov A., 1999, ApJ, 516, 530
 Kravtsov A.V., Klypin A.A., 1999, ApJ, 520, 437
 Lewis I.J., et al., 2002, MNRAS, 333, 279
 Mathis H., Lemson G., Springel V., Kauffmann G., White S.D.M., Eldar A., Dekel A., 2002, MNRAS, 333, 739
 Moore B., 2001, in Wheeler J.C., Martel H., eds, Proc. AIP Conf. Vol. 586, Proceedings of the Texas Symposium. Am. Inst. Phys., New York, p. 73
 Peacock J.A., Dodds S.J., 1996, MNRAS, 280, L19
 Pearce F.R., Jenkins A., Frenk C.S., White S.D.M., Thomas P.A., Couchman H.M.P., Peacock J.A., Efsthathiou G., 2001, MNRAS, 326, 649.
 Pen U.-L., 1997, ApJ, 490, L127
 Percival W.J., et al., 2001, MNRAS, 327, 1297
 Press W.H., Schechter P., 1974, ApJ, 187, 425
 Saunders W., et al., 2000, MNRAS, 317, 55
 Seljak U., 2000, MNRAS, 318, 203
 Sheth R.K., Jain B., 2002, submitted to MNRAS. (astro-ph/0208353)
 Somerville R.S., Lemson G., Sigad Y., Dekel A., Kauffmann G., White S.D.M., 2001, MNRAS, 320, 289
 Wang X., Tegmark M., Zaldarriaga M., 2002, Phys. Rev. D 65, 123001
 White S.D.M., Frenk C.S., 1991, ApJ, 379, 52
 White M., Hernquist L., Springel V., 2001, ApJ, 550, L129
 York D.G. et al., 2000, AJ, 120, 1579
 Yoshikawa K., Taruya A., Jing Y.P., Suto Y., 2001, ApJ, 558, 520
 Zehavi, I., et al., 2002, ApJ, 571, 172
 Zehavi, I., et al., 2003, submitted to ApJ. (astro-ph/0301280)